Fatigue Study of the Pre-Corroded 6082-T6 Aluminum Alloy in Saline Atmosphere

Alejandro Fernández Muñoz [1], José Luis Mier Buenhombre [2,*], Ana Isabel García-Diez [2], Carolina Camba Fabal [2] and Juan José Galán Díaz [2]

[1] Navantia, Polígono Astilleros, S/N, 11519 Puerto Real, Spain; alfemu78@hotmail.com
[2] Escuela Politécnica Superior, University of A Coruña, Mendizábal s/n, 15403 Ferrol, Spain;
    ana.gdiez@udc.es (A.I.G.-D.); ccamba@udc.es (C.C.F.); juan.jose.galan@udc.es (J.J.G.D.)
* Correspondence: jose.mier@udc.es; Tel.: +34-881-013-268

Abstract: This work studies the influence of the saline atmospheric corrosion on the fatigue strength of 6061-T6 aluminum alloy. For this purpose, this alloy was subjected to tests in a salt spray corrosion chamber at different exposure times (1, 2, and 3 months) according to ASTM B117 standard. The morphological study of the pits was carried out by confocal microscopy. Subsequently, fatigue tests were performed at variable stresses whose maximum stress (S_{max}) was between 30% and 95% of the yield strength (S_0) in order to keep them within the zone of elastic behavior of the material. Data were analyzed using the Basquin equation and the maximum likelihood function method. The results show a similar decrease in the conventional fatigue limit (2×10^6 cycles) after one month (98 MPa) and two months (91 MPa) of corrosion. After three months of corrosion, the material showed a very important reduction in the fatigue limit (68 MPa) with respect to the uncorroded material (131 MPa). The data of S_e/S_0 (fatigue limit/yield strength) versus the ratio P_m/D_m (pit average depth/pit diameter at zero depth) can be fitted to a logarithmic curve.

Keywords: 6061-T6 aluminum alloy; pitting; confocal microscopy; fatigue; Basquin's equation; maximum likelihood method

1. Introduction

Aluminum alloys have great advantages in shipbuilding and offshore platforms applications thanks to their lightweight, specific strength, and corrosion resistance. AlMg (series 5xxx) and AlMgSi (series 6xxx) are the most commonly used aluminum alloys in seawater [1]. One of them is 6061 alloy, which is used for general purposes in the form of extruded profiles because the combination of mechanical properties and adequate corrosion resistance makes it one of the most versatile aluminum alloys in marine applications. Its good mechanical properties are due to the aging treatment, which can be natural (T4) or artificial (T6). 6061 aluminum alloys have %Mg + %Si (wt) in amounts greater than 1.4%, which favors the increase in mechanical resistance after heat treatment compared with other alloys such as 6063. Magnesium and silicon form Mg_2Si compound, which behaves like a semiconductor [2,3]. Additionally, it contains amounts of Cu around 0.25% to improve corrosion resistance and 0.7% Fe, which results in the precipitation of the ternary compounds $Al_xFe_ySi_z$ [4,5]. All these types of precipitates favor the appearance of localized corrosion due to the difference in electrochemical potentials between them and the matrix [6,7]. 6061 alloy is less resistant to pitting corrosion than non-aging AlMg alloys, especially in T6 condition, in the presence of chloride ions and poorly aerated deep water with low pH. The study of pitting corrosion can be carried out according to the ASTM G46 standard [8] to determine the morphology, density, size, and depth of the pits and to predict the remaining service life of the alloy. According to this standard, the pitting factor (F_p) can be calculated

by dividing the deepest metal penetration by the average metal penetration when corrosion is uniform. One instrumental way to parameterize the pits is to use confocal microscopy. This technique is an extension of conventional microscopy, which allows to perform the three-dimensional characterization of the materials' surface and is a very interesting non-contact technique for the study of pitting as it is possible to obtain finer details of the morphology of a surface because of its higher lateral resolution.

In addition, it is important to take into account that marine structures may be subject to cyclical loads of different nature. The formation of pits has a detrimental effect on the fatigue strength aluminum alloy. Pits can be cracking nuclei under cyclic loads that can compromise structural integrity as a result of the effect of stress concentration [9–11]. There are situations in which the structures of 6061-T6 alloys can be corroded by the effect of the saline atmosphere and subsequently be subjected to cyclic stresses of low intensity and high frequency (vibrations) and high intensity and low frequency (waves). In the former, failure can occur after a high number of cycles, while in the latter, fracture occurs at a much lower number of cycles. There are many studies that have determined the influence of pitting on the fatigue strength of aluminum alloys [12–15]. However, little has been investigated on the fatigue behavior of AlMgSi alloys in the presence of a high salt concentration. The objective of this work is to provide information on the resistance to fatigue of this type of alloy in the extreme environments mentioned, given that many of the applications of these alloys require good performance in saline atmospheres.

The present research was carried out in two stages. Firstly, the pits generated in a highly saline environment were dimensionally characterized in order to evaluate the main pitting parameters. Secondly, the relationship between the severity of pitting and the decrease of fatigue strength was analyzed.

2. Materials and Methods

Sheets of 6082-T6 alloy with 2 mm of thickness were used. The composition (%wt) of this material is as follows: 0.7–1.2% Si, 0.6–1.2% Mg, 0.4–1.0% Mn, 0.50% Fe, 0.10% Cu, 0.25% Cr, 0.20% Zn, and 0.10% other elements, Al balance. Before any test, the material was machined according to the ASTM E-8/E 8M-08 standard [16] to obtain the samples used throughout this work. Its dimensions are shown in Figure 1. The orientation of the samples was chosen so that the main axis of the specimen was parallel to the direction of rolling.
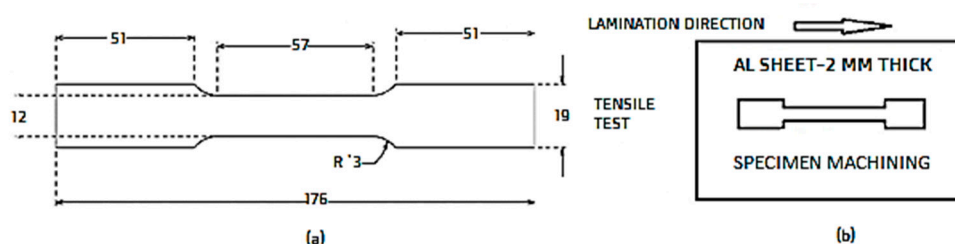
Figure 1. (**a**) Dimensions of the specimens (in mm) used in the tensile test and fatigue test, (**b**) orientation of the specimens with respect to the rolling direction of the metal sheets.

The corrosion tests were carried out in a salt spray chamber DYCOMETAL SSC 400 (DYCOMETAL EQUIPOS CONTROL DE CALIDAD, S.L., Barcelona, Spain) according to ASTM B117 standard [17]. According to this standard, the salt solution was prepared by dissolving 5 parts by mass of sodium chloride (Merck, Darmstadt, Germany) in 95 parts of water. The salt used contained, as set by the standard, less than 0.3% by mass of total impurities. The pH of the saline solution was 6.5, the saline concentration was 15%, and the pressure was between 0.9 and 1.0 bar. The temperature inside the chamber was 35 °C. The samples were corroded for 1 month (C1), 2 months (C2), and 3 months (C3). The loss of mass due to corrosion was determined with a SCALTEC precision scale model SBC 22 (SCALTEC Instruments GmbH, Goettingen, Germany) with an accuracy of 0.01 mg.

Weight measurements were made before and after the corrosive attack and carefully removing impurities on the surface. The analysis of the corrosion products was done with a D5000 SIEMENS X-ray diffractometer (SIEMENS, Munich, Germany). The Diffractplus V.8.0 (8.0, Bruker AXS Advanced X-ray Solutions GmbH, Karlsruhe, Germany) and Bruker-AXS (Bruker AXS Advanced X-ray Solutions GmbH, Karlsruhe, Germany) software programs were used for data acquisition and processing.

Morphological studies of the pits were performed by confocal microscopy using a Sensofar PLμ 2300 dual microscope (SENSOFAR, Terrassa, Spain). The acquisition of data was done using the Gwyddion (Czech Metrology Institute, Brno, Czech Republic) and SensoMAP (SENSOFAR, Terrassa, Spain) computer packages. Scanning electron microscopy (SEM) image was obtained by a JEOL JSM 6400 microscope (JEOL, Tokio, Japan).

The equipment used for the tensile and fatigue tests was a servo-hydraulic universal testing machine Instron 8800 with Fast Track controller (Instron, Norwood, Massachusetts, MA, USA). Axial stresses were applied in the direction of alloy rolling. The software used for the tests design is WaveMaker (WaveMaker, Inc.,Mountain View, California, CA, USA). The 100 kN load cell has a force relative error over the entire measurement range of 0.22%. The temperature and humidity conditions were environmental. The oxide layer of the test samples was not removed in both kinds of tests in order to obtain similar conditions to those of service of the material. Therefore, the tests are carried out with the surface in the same conditions that are presented in service, without previously treating them. The fatigue tests were carried out by applying a periodic axial load of constant stress amplitude with a stress ratio ($R = S_{min}/S_{max}$) of 0.1 and a frequency of 15 Hz. As a criterion for the end of these tests, the fracture of the samples or conventional fatigue limit at 2×10^6 cycles were considered [18–20] (the end of the test is set to this value for those samples that were not previously broken). The maximum stress values (S_{max}) were between 30% and 95% of the elastic limit, in order to keep them within the zone of elastic behavior of the material. A minimum of four S_{max} values and three samples in each S_m level were tested for each corrosion time. The results were divided into two groups in order to evaluate separately the slope of the S–N curve between 10^3 and 10^6 cycles by the Basquin method [21–23] and the fatigue limit (S_e) by the maximum likelihood function method [24–27]. Starting from a data sample, the objective of the likelihood method is to find the population with the highest probability of having generated this sample. A detailed explanation of this statistical method, widely used in parameter estimation, has been published by Myung in 2003 [28].

3. Results and Discussion

Figure 2a shows the three-dimensional representation of the uncorroded material obtained by confocal microscopy where rolling grooves in the *x* direction can be seen. Furthermore, microcracks can also be perceived by scanning electron microscope (Figure 2b). They have a depth of approximately 10 μm and their formation may be due to the rolling process. These microcracks are not evenly distributed over the surface, but appear very localized. These defects may constitute anodic zones where pitting corrosion can be intense, and thus reduce the fatigue strength of the material.
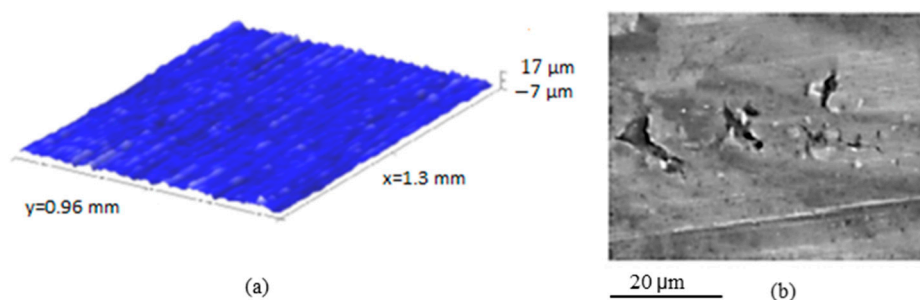
Figure 2. (**a**) Image of the surface texture of the uncorroded alloy, where *x* axis represents the rolling direction, (**b**) scanning electron microscopy (SEM) image showing the rolling microcracks.

As an example of calculating the pitting parameters, see Figure 3 obtained by confocal microscopy from a sample corroded for two months. The maximum depth (P) is 20.5 µm and the mean diameter (D) at zero level is 40 µm. If it is considered that the pit can approach an elliptical geometry in depth, the P/D ratio gives information on the concentration of stresses at the bottom of the notch and the severity of the defect. In this way, P represents the major axis of the ellipse and D is the minor. If the value of D approaches zero, the stress value at the bottom of the pit becomes infinite (ideal crack).
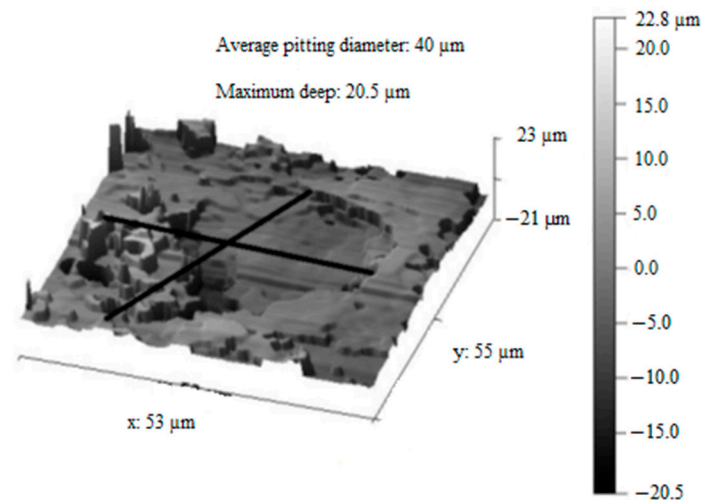
Figure 3. Two-dimensional digital image of a pit of the sample corroded during two months (C2) obtained by confocal microscopy. Pit depth and mean diameter were determined by Sensomap software.

The average parameters were determined by confocal microscopy for a total area of the confocal image (A_{imla_conf}) of 33 mm^2. These parameters can be seen in Table 1, where ρ_p is pit density, F_p is the pitting factor, P_m is the average pit depth, D_m is the average pit diameter measured at the surface, and P_{max} is the deepest pit value detected. Pits with a depth superior to 10 µm were chosen for the calculation of the values, as it was intended to conduct the study without taking into account the lamination defects. In Figure 4, the normal distribution of the depth (a) and diameter (b) of the pit can be observed. It can be seen how both the diameter and the depth of the pit are greater for samples C1 and C2 than for C3, although the difference is greater in the case of depth. It can also be seen how the depth of the pit increases significantly the longer the exposure time. This trend is also observed in the case of diameter, but again in a less pronounced way.

Table 1. Parameters determined by confocal microscopy for a total area (A_{imla_conf}) of 33 mm^2 where ρ_p is pit density, P_{max} is the deepest pit value detected, P_m is the average pit depth, σ_{Pm} is the standard deviation of P_m, D_m is the average pit diameter measured at surface, σ_{Dm} is the standard deviation of D_m, and F_p is the pitting factor.

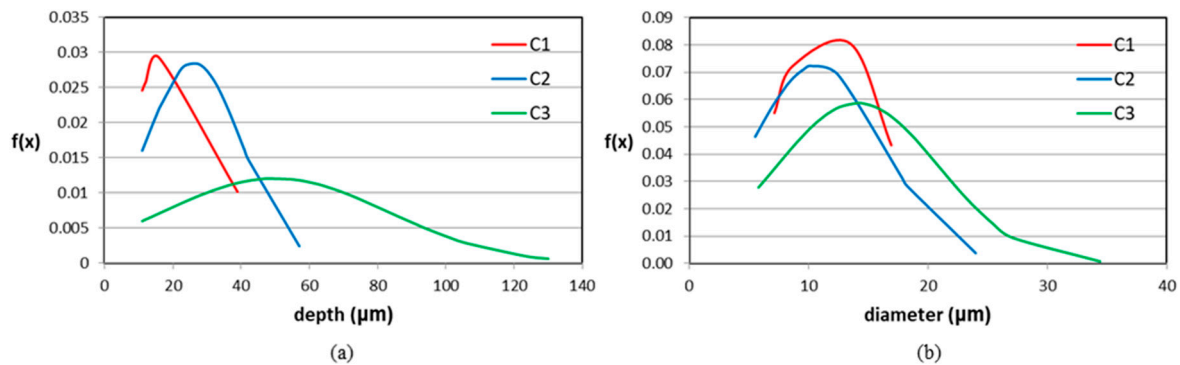| Parameter	C1	C2	C3
ρ_p (pic/mm^2)	0.12	0.44	1.25
P_{max} (µm)	39	57	130
P_m (µm)	19.5	26.0	50.0
σ_{Pm}	13.2	14.1	33.0
D_m (µm)	11.5	10.9	14.1
σ_{Dm}	4.5	5.5	6.8
$(P/D)_m$	1.61	2.35	3.27
F_p	2.00	2.19	2.60

Figure 4. Normal distribution of the depth (**a**) and diameter (**b**) of the pit.

Table 1 shows that the pitting parameters increase with corrosion time, especially in C3 specimens. The pit density (ρ_p) is tripled each month or, what is the same, there is a constant speed of pits appearance on the surface of the alloy. Taking into account that the F_p factor is 1.00 when there is uniform corrosion, there is a high degree of localized attack from the first month of testing ($F_p = 2.00$); in particular, the pitting severity increases considerably from the third month of testing. There is also an increase in the $(P/D)_m$ ratio with the corrosion time, although the average pit diameter (D_m) has hardly changed during the first two months in sample C2. On the other hand, the values of the maximum depth of pitting (P_{max}) have to be taken into account for the estimation of the maximum net section stress that supports the material, that is, considering only the uncracked cross section of the sample.

The results of the X-ray diffraction (XRD) analyses were similar in all samples. Figure 5 shows the diffractograms of the samples C1 (black line), C2 (red line), and C3 (blue line), respectively. The oxidation product layer consists mainly of bayerite [β-Al(OH)$_3$. 3H$_2$O]. In the case of sample C3, more intense bayerite peaks were obtained than in the other samples, indicating a higher level of corrosion. Bayerite is a metastable compound that constitutes an intermediate stage between amorphous aluminum hydroxide and gibbsite [29]. The last one is a common compound in the atmospheric corrosion of aluminum alloys, especially when there are alkaline ions in the medium [30].
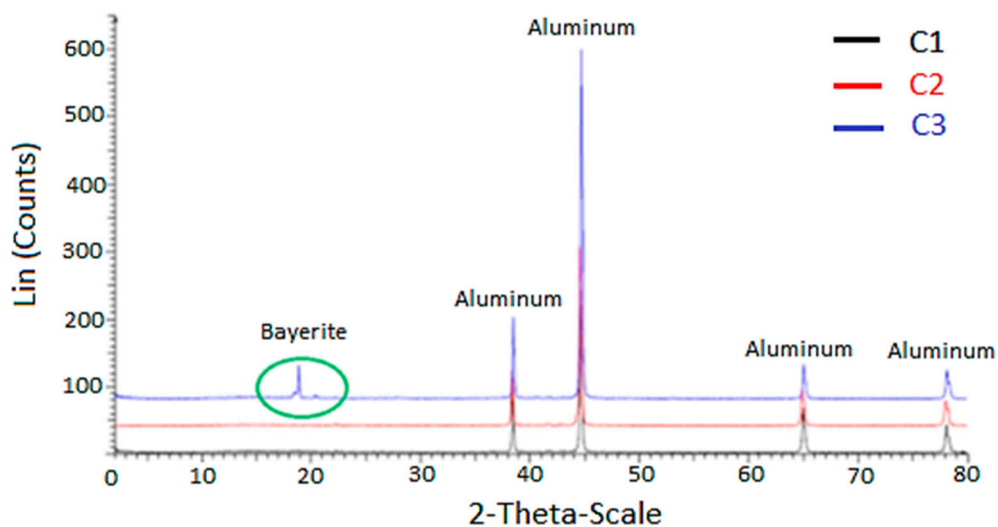

Figure 5. X-ray diffraction analysis of corrosion products where a bayerite [β-Al(OH)$_j$. 3H2O] peak can be seen in the sample corroded for 3 months.

The tensile tests are shown in Figure 6. The data obtained for the tensile strength (S_u) and yield strength (S_0) of the uncorroded material (R) match the values found in the literature (see Table 2):

311 MPa for S_u and 275 MPa for S_0. In the corroded samples C1 and C2, S_u and S_0 do not change with respect to the uncorroded material. By last, there is a decrease in the tensile strength for the corroded samples during 3 months (C3). In this case, S_u falls to 286 MPa, 8% lower than the R value, and its yield strength decreases to 255 MPa, 7% less than in R. Defining the value of S_0 for each type of sample is very important because it will be used as a reference stress in the subsequent fatigue tests of this work. The elongation (ε_f) is the parameter most sensitive to the corrosion process, as can be seen in Figure 6. It is around 17% for the uncorroded material, 15.5% for C1, and approximately 11% for C2 and C3. According to these results, it can be deduced that, from the first month of corrosion, the ductility decreases significantly.
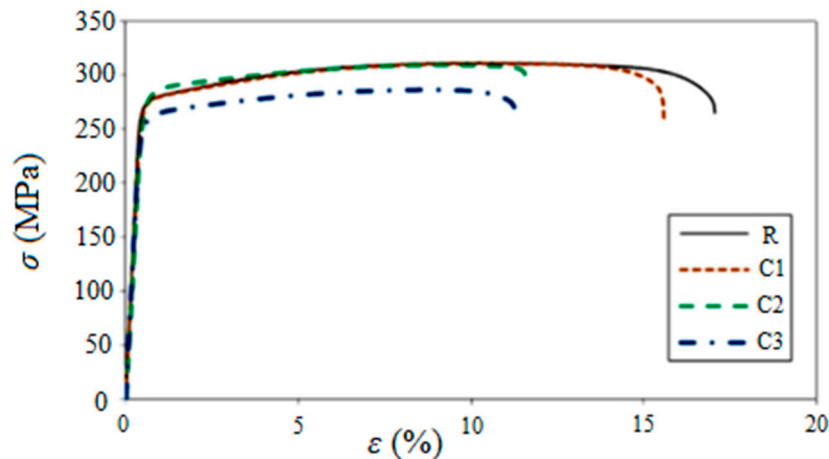
Figure 6. Tensile curves of the uncorroded and corroded samples.

Table 2. Yield stress, tensile strength, and elongation values obtained from Figure 6.

Material	S_0 (MPa)	S_u (MPa)	ε_f
Uncorroded (R)	275	311	17.0
C1	271	311	15.5
C2	276	309	11.6
C3	255	286	11.2

The adjustment of the S/N curves by the Basquin method was performed using the maximum stresses of 95% S_0, 90% S_0, 80% S_0, and 70% S_0 in the case of the uncorroded material (R) and 95% S_0, 70% S_0, 55% S_0, and 45% S_0 in the corroded samples. This adjustment is equivalent to expressing fatigue strength as a straight line of slope b in an S/N diagram in double logarithmic scale.

$$\Delta S = KN^b \tag{1}$$

K represents the stress required to produce fracture when only one stress cycle is applied and b is the Basquin exponent, which characterizes how much the number of cycles varies until fracture with the change of alternating tension. b is in the range of −0.05 to −0.12 for most uncorroded metals [31,32].

Figure 7 shows the ΔS versus N graph that collects the average experimental data shown in Table 3, with a logarithmic scale for the x and y axes, together with the adjustments obtained for each sample. There is a significant decrease in fatigue strength when corrosion is only one month. Meanwhile, the changes are more appreciable for a high number of cycles between the state C1 and C2. In the case of C3, the curve begins at a lower stress level because its elastic limit is lower than the rest of the materials, and testing at a higher level could have masked the fatigue crack growth process with a process of high plastic deformation.
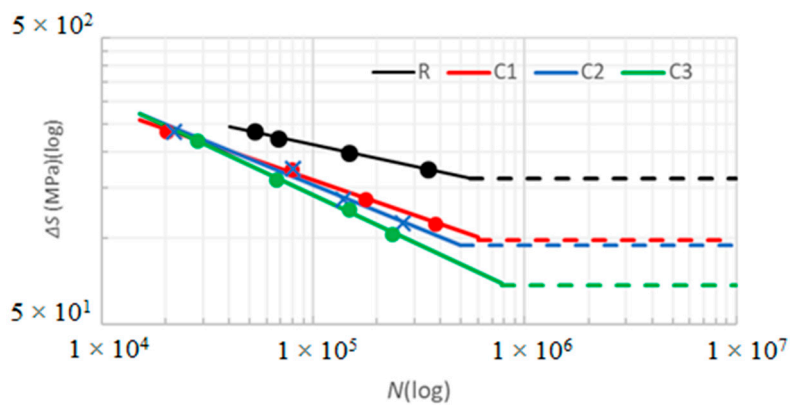
Figure 7. Stress range (ΔS) vs. average number of cycles at failure (N) curve.

Table 3. Data of stress range (ΔS) and average number of cycles at failure (N) for S_{max}/S_0 ratios tested. σ is the standard deviation of N data and (%σ) standard deviation expressed as percentage.

| Sample	S_{max}/S_0	ΔS (MPa)	N (cycles)	σ	σ (%)
R	0.95	235	52,432	20,813	40
	0.90	223	68,404	29,931	44
	0.80	198	147,233	7945	5
	0.70	174	348,293	191,183	55
C1	0.95	235	20,248	4129	20
	0.70	174	78,343	18,991	24
	0.55	136	175,615	35,238	20
	0.45	112	376,934	134,688	36
C2	0.95	235	21,944	2789	13
	0.70	174	79,986	7991	10
	0.55	136	138,925	14,744	11
	0.45	112	264,567	23,102	9
C3	0.95	218	28,266	5367	19
	0.70	160	66,757	15,519	23
	0.55	126	148,015	50,770	34
	0.45	103	236,728	89,123	38

Table 4 includes the fatigue strength coefficient (K), the Basquin exponent (b), and the coefficient of determination (R^2). The coefficient of determination is 0.98 for sample C2, while it is higher than 0.99 for C1 and C3, which is indicative that the number of stress values used is sufficient for a high approximation of the Basquin equation. In relation to the coefficient K, an increase is obtained with the severity of the pits, given by the P/D ratio, especially between R and C1. Similarly, the Basquin exponent (b) shows a significant decrease from the first month of corrosion.

Table 4. Fitting constants of the Basquin equation.

Material	K (MPa)	B	R^2
R	1.287	−0.1570	0.999
C1	3.008	−0.2557	0.996
C2	4.846	−0.3002	0.983
C3	7.495	−0.3453	0.997

Applying Basquin's equation for the value of 200 MPa, it is calculated that the life (N) for the uncorroded material (R) is 141,251 cycles, while for C1 and C2, it decreases to approximately 42,000 cycles, which represents a decrease with respect to R of almost 72% (Figure 8). In the case of C3, N is

36,108 cycles, which is a 74% decrease with respect to *R*. Thus, there is a clear decrease in fatigue strength with corrosion time and the highest difference is between the uncorroded material (*R*) and the corroded material during one month (C1). When ΔS is 150 MPa, the number of cycles to failure is 882,630 for *R*, while it is 123,775 and 106,567 cycles for C1 and C2, respectively, which represents a decrease in relation to *R* of approximately 86% for C1 and 88% for C2. The material in state C3 has a decrease of N_f of 91% compared with *R*.
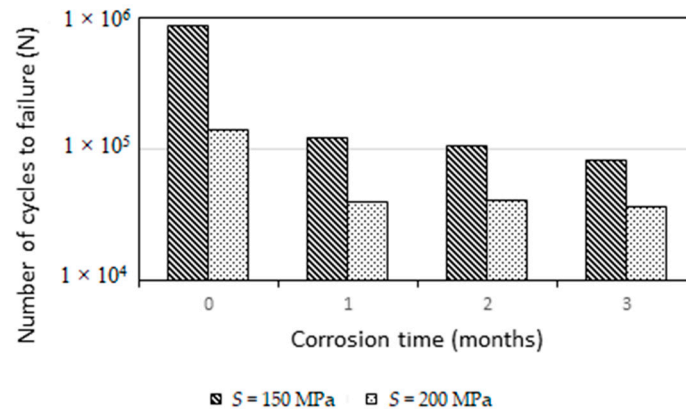
Figure 8. Number of cycles to failure (*N*) vs. corrosion time (*t*). Data were calculated from the Basquin equation for ΔS = 200 MPa (dark) and ΔS = 100 MPa (light).

The adjustment of the S/N curves by the maximum likelihood method was performed for the maximum stress levels 65% σ_0 and 55% σ_0 in the case of *R*, 40% σ_0 and 35% σ_0 in C1 and C2, and 40% σ_0 and 35% σ_0 in C3. This method assumes that the runouts test stress is distributed normally for a certain number of cycles [33]. The probability of experimental data is given by

$$V = \prod_{i=1}^{n} [1 - F(S_i, \bar{x}, \sigma)]^{r_i} [1 - F(S_i, \bar{x}, \sigma)]^{f_i} \tag{2}$$

where $\bar{x}$ is the mean, σ is the standard deviation, r_i represents the number of "run-outs" at the ith stress level (S_i), f_i is the number of failures observed at the same stress level, and *F* is the cumulative probability of failure. This equation can be written as

$$F(S, \bar{x}, \sigma) = \int_{-\infty}^{S} \frac{1}{\sigma \sqrt{2\pi}} exp\left[-\frac{1}{2}\left(\frac{\bar{x} - x}{\sigma}\right)^2\right] dx \tag{3}$$

Equation (2) in the form of napierian logarithms is expressed as

$$lnV = \sum_{i=1}^{n} r_i ln(1 - F_i) + f_i lnF_i \tag{4}$$

where F_i is $F(S_i, \bar{x}, \sigma)$. It is necessary to obtain the partial derivatives with respect to $\bar{x}$ *y* σ and equate them to zero to calculate the maximum of Equation (4). Thus, a system of two non-linear equations with two unknowns $\bar{x}$ *y* σ is obtained. The resolution of the system makes it possible to calculate the fatigue limit and the associated deviation.

Table 5 shows the results of the fatigue limit S_e and the percentage deviation (σ%) calculated considering a technological life level of 2×10^6 cycles. The value obtained for the fatigue limit of sample *R* is 161 MPa. In the case of C1, the limit is 98 MPa, which implies a reduction in the fatigue limit of 39%. In the same way as in the analysis of fatigue strength, it is in this first stage of corrosion that the most pronounced reduction in fatigue response occurs. The decrease in fatigue limit is not so

marked between C1 and C2 (94 MPa). However, the C3 samples corroded for three months show a large decrease of S_e (68 MPa) with respect to the previous stage samples (C2). The total decrease of S_e between material R and C3 was 57.4%. The drastic decrease in fatigue resistance during the first month of saline corrosion is in accordance with studies carried out by other authors [12], in which it was observed that the corrosive effect has a more pronounced effect on aged aluminum alloys, such as alloy 6061-T6, than non-heat treatable aluminum alloys (2xxx, 5xxx groups).

Table 5. Fatigue limit (S_e), and the percentage deviation ($\sigma\%$) calculated considering a technological life level of 2×10^6 cycles.

Material	$\%S_0$	S_{max} (MPa)	F	r	S_e (MPa)	σ (%)
R	65	161	6	3	161	1.55
	55	151	0	3		
C1	40	99	2	1	98	1.47
	35	86	0	3		
C2	40	99	4	0	94	0.21
	35	86	0	3		
C3	35	68	2	1	68	0.76
	27	62	0	3		

Figure 9 shows the fatigue parameter S_e/S_0 versus $(P/D)_m$ ratio for R, C1, C2, and C3 samples. The point corresponding to the reference material (uncorroded sample) does not start from $P_m/D_m = 0$, but from 8.6 μm/74 μm = 0.11. This is explained by the presence of microcracks resulting from the lamination process. The maximum depth observed in these microcracks was 10 μm. This graph shows that all data can be correlated by a logarithmic curve. The determination coefficient (R^2) is 0.985, which indicates a good fit. This demonstrates that a correlation can be established between a dimensional ratio of the pits $(P/D)_m$ and the normalized fatigue limit (S_e/S_0), allowing even to integrate the uncorroded material data into the fit. This result makes sense considering that the ratio $(P/D)_m$ is indicative of the concentration of stresses at the edge of the pit, reducing the fatigue strength of the material. According to various authors [34,35], the significant decrease in fatigue strength in precorroded aluminum alloys is related to the progressive appearance of pits, which are stress concentration points where cracks begin.
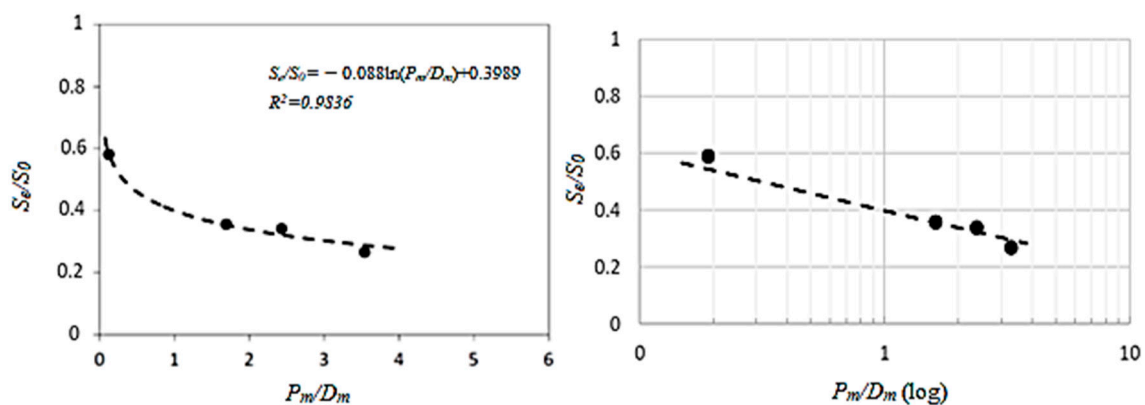
Figure 9. Fatigue S_e/S_0 ratio vs. $(P/D)_m$ ratio for R, C1, C2, and C3 samples.

4. Conclusions

Corrosion parameters show a large increase after 3 months in a salt spray chamber. Pitting factor (F_p) values indicate that corrosion is highly localized from the first month. X-ray diffraction analysis shows the formation of aluminum hydroxides: bayerite. The appearance of intense bayerite peaks at the third month of corrosion (C3) is related to a higher level of corrosion.

The samples corroded for three months (C3) are the most affected in the tensile test. In this case, tensile strength (S_u) falls to 286 MPa, 8% lower than the uncorroded material value, and its yield strength (S_0) decreases to 255 MPa, 7% less than in R. On the other hand, the results show a significant decrease in ductility from the first months of corrosion.

The application of the Basquin equation and the maximum likelihood model shows a significant decrease in the number of cycles until failure during the first month of corrosion (around 72% for C1 when ΔS is 200 MPa, and 86% when ΔS is 150 MPa). This decrease continues for the next two months (C2 and C3), but without the variations being so marked with respect to C1.

Finally, the fatigue data were treated with the maximum likelihood model. The conventional fatigue limit suffers an important decrease between R (161 MPa) and C1 (98 MPa) and between C2 (94 MPa) and C3 (68 MPa). The representation of the fatigue parameter S_e/S_0 versus ratio P_m/D_m ratio shows that data can be correlated by a logarithmic curve. The determination coefficient (R^2) is 0.985, which indicates a good fit.

References

1. Al-Moubaraki, A.H.; Al-Rushud, H. The Red Sea as a corrosive Environment: Corrosion Rates and corrosion mechanism of aluminum alloys 7075, 2024, and 6061. *Int. J. Corros.* **2018**, *2018*, 2381287. [CrossRef]

2. Mizoguchi, H.; Muraba, Y.; Fredrickson, D.C.; Matsuishi, S.; Kamiya, T.; Hosono, H. The unique electronic structure of Mg2Si: Shaping the conduction bands of semiconductors with multicenter bonding. *Angew. Chem.* **2017**, *56*, 10135–10139. [CrossRef] [PubMed]

3. Kaur, K.; Ranjan, K. Electronic and thermoelectric properties of Al doped Mg2Si material: DFT study. *Mater. Today Proc.* **2016**, *3*, 1785–1791. [CrossRef]

4. Couper, M.J.; Rinderer, B.; Yao, J.Y. Characterisation of AlFeSi intermetallics in 6000 series aluminium alloy extrusions. *Mater. Sci. Forum* **2006**, *519–521*, 303–308. [CrossRef]

5. Prillhofer, R.; Rank, G.; Berneder, J.; Antrekowitsch, H.; Uggowitzer, P.J.; Pogatscher, S. Property criteria for automotive Al-Mg-Si sheet alloys. *Materials* **2014**, *7*, 5047–5068. [CrossRef] [PubMed]

6. Linardi, E.; Haddad, R.; Lanzani, L. Stability analysis of the Mg2Si phase in AA 6061 aluminum alloy. *Procedia Mater. Sci.* **2012**, *1*, 550–557. [CrossRef]

7. Zhu, M.; Zhao, B.Z.; Yuan, Y.F.; Guo, S.Y.; Pan, J. Effect of Solution Temperature on the Corrosion Behavior of 6061-T6 Aluminum Alloy in NaCl Solution. *J. Mater. Eng. Perform.* **2020**, *29*, 4725–4732. [CrossRef]

8. ASTM G46-94. *Standard Guide for Examination and Evaluation of Pitting Corrosion*; ASTM International: West Conshohocken, PA, USA, 2018.

9. McAdam, D.J., Jr. Stress-Strain-Cycle Relationship and Corrosion-Fatigue of Metals. *Proc. ASTM* **1926**, *26*, 224–280.

10. Cerit, M.; Genel, K.; Eksi, S. Numerical investigation on stress concentration of corrosion pit. *Eng. Fail. Anal.* **2009**, *16*, 2467–2472. [CrossRef]

11. Horner, D.A.; Connolly, B.J.; Zhou, S.; Crocker, L.; Turnbull, A. Novel images of the evolution of stress corrosion cracks from corrosion pits. *Corros. Sci.* **2011**, *53*, 3466–3485. [CrossRef]

12. Yang, H.; Wang, Y.; Wang, X.; Pan, P.; Jia, D. The effects of corrosive media on fatigue performance of structural aluminum alloys. *Metals* **2016**, *6*, 160. [CrossRef]

13. Sankaran, K.K.; Perez, R.; Jata, K.V. Effects of pitting corrosion on the fatigue behavior of aluminum alloy 7075-T6: Modeling and experimental studies. *Mater. Sci. Eng. A* **2001**, *297*, 223–229. [CrossRef]

14. Genel, K. The effect of pitting on the bending fatigue performance of high-strength aluminum alloy. *Scr. Mater.* **2007**, *57*, 297–300. [CrossRef]

15. Zupanc, U.; Grum, J. Effect of pitting corrosion on fatigue performance of shot-peened aluminium alloy 7075-T651. *J. Mater. Process. Technol.* **2010**, *210*, 1197–1202. [CrossRef]

16. ASTM E8/E8M. *Standard Test Methods for Tension Testing of Metallic Materials*; ASTM International: West Conshohocken, PA, USA, 2008.

17. ASTM B117. *Standard Practice for Operating Salt Spray (Fog) Apparatus*; ASTM International: West Conshohocken, PA, USA, 2019.

18. Saga, M.; Kopas, P.; Uhricik, M. Modeling and experimental analysis of the aluminium alloy fatigue damage in the case of bending–torsion Loading. *Procedia Eng.* **2012**, *48*, 599–606. [CrossRef]

19. Calcraft, R.C.; Schumann, G.O.; Viano, D.M. Fatigue of marine grade aluminium alloys. *Aust. Weld. J.* **1997**, *42*, 22–25.

20. Gaya, A.; Lefebvre, F.; Bergamo, S.; Valiorgue, F.; Chalandond, P.; Michel, P.; Bertrand, P. Fatigue of aluminum/glass fiber reinforced polymer composite assembly joined by self-piercing riveting. *Procedia Eng.* **2015**, *133*, 501–507. [CrossRef]

21. Basquin, O.H. The exponential law of endurance tests. *Am. Soc. Test. Mater. Proc.* **1910**, *10*, 625–630.

22. Ren, C.X.; Wang, D.Q.Q.; Wang, Q.; Guo, Y.S.; Zhang, Z.J.; Shao, C.W.; Yang, H.J.; Zhang, Z.F. Enhanced bending fatigue resistance of a 50CrMnMoVNb spring steel with decarburized layer by surface spinning strengthening. *Int. J. Fatigue* **2019**, *124*, 277–287. [CrossRef]

23. Hong, S.; Weil, R. Low cycle fatigue of thin copper foils. *Thin Solid Film.* **1996**, *283*, 175–181. [CrossRef]

24. McCool, J.I. Evaluating Weibull endurance data by the method of maximum likelihood. *ASLE Trans.* **1970**, *13*, 189–202. [CrossRef]

25. Spindel, J.E.; Haibach, E. The method of maximum likelihood applied to the statistical analysis of fatigue data. *Int. J. Fatigue* **1979**, *1*, 81–88. [CrossRef]

26. Marquis, G.; Mikkola, T. Analysis of welded structures with failed and non-failed welds based on maximum likelihood. *Weld. World* **2002**, *46*, 15–22. [CrossRef]

27. Lorén, S.; Lundström, M. Modelling curved S-N curves. *Fatigue Fract. Eng. Mater. Struct.* **2005**, *28*, 437–443. [CrossRef]

28. Myung, I.J. Tutorial on maximum likelihood estimation. *J. Math. Psychol.* **2003**, *47*, 90–100. [CrossRef]

29. Setiadi, A.; Milestone, N.B.; Hill, J.; Hayes, M. Corrosion of aluminum and magnesium in BFS composite cements. *Adv. Appl. Ceram.* **2006**, *105*, 191–196. [CrossRef]

30. Zhang, J.; Klasky, M.; Letellier, B.C. The aluminum chemistry and corrosion in alkaline solutions. *J. Nucl. Mater.* **2009**, *384*, 175–189. [CrossRef]

31. Haidemenopoulos, G.N. *Physical Metallurgy: Principles and Design*; CRC Press: Boca Raton, FL, USA, 2018.

32. Kun, F.; Carmona, H.; Andrade, J.S.; Herrmann, H.J. Universality behind Basquin's Law of Fatigue. *Phys. Rev. Lett.* **2008**, *100*, 094301. [CrossRef]

33. Engler-Pinto, C.C., Jr.; Lasecki, J.V.; Frisch, R.J., Sr.; Allison, J.E. Statistical approaches applied to very high cycle fatigue. In *Proceedings of the Fourth International Conference on Very High Cycle Fatigue (VHCF-4), Ann Arbor, MI, USA, 19–22 August 2007*; Allison, J.E., Jones, J.W., Larsen, J.M., Ritchie, R.O., Eds.; TMS (The Minerals, Metals & Materials Society): Warrendale, PA, USA, 2007; pp. 369–376.

34. Jones, K.; Hoeppner, D.W. Prior corrosion and fatigue of 2024-T3 aluminum alloy. *Corros. Sci.* **2006**, *48*, 3109–3122. [CrossRef]

35. Chen, G.S.; Liao, C.M.; Wan, K.C.; Gao, M.; Wei, R.P. Pitting corrosion and fatigue crack nucleation. *ASTM Spec. Tech. Publ.* **1997**, *1298*, 18–32.